
Boundary Graph Neural Networks for 3D Simulations

Andreas Mayr
ELLIS Unit Linz, LIT AI Lab
Johannes Kepler University Linz
mayr@ml.jku.at

Sebastian Lehner
ELLIS Unit Linz, LIT AI Lab
Johannes Kepler University Linz

Arno Mayrhofer
DCS Computing GmbH
Linz, Austria

Christoph Kloss
DCS Computing GmbH
Linz, Austria

Sepp Hochreiter
ELLIS Unit Linz, LIT AI Lab
Johannes Kepler University Linz
Institute of Advanced Research in
Artificial Intelligence (IARAI)

Johannes Brandstetter
University of Amsterdam
ELLIS Unit Linz, LIT AI Lab
Johannes Kepler University Linz
brandstetter@ml.jku.at

Abstract

The abundance of data has given machine learning huge momentum in natural sciences and engineering. However, the modeling of simulated physical processes remains difficult. A key problem in doing so is the correct handling of geometric boundaries. While triangularized geometric boundaries are very common in engineering applications, they are notoriously difficult to model by machine learning approaches due to their heterogeneity with respect to size and orientation. In this work, we introduce Boundary Graph Neural Networks (BGNNs), which dynamically modify graph structures to address boundary conditions. Boundary graph structures are constructed via modifying edges, augmenting node features, and dynamically inserting virtual nodes. The new BGNNs are tested on complex 3D granular flow processes of hoppers and rotating drums which are standard parts of industrial machinery. Using precise simulations that are obtained by an expensive and complex discrete element method, BGNNs are evaluated in terms of computational efficiency as well as prediction accuracy of particle flows and mixing entropies. Even if complex boundaries are present, BGNNs are able to accurately reproduce 3D granular flows within simulation uncertainties over hundreds of thousands of simulation timesteps, and most notably particles completely stay within the geometric objects without using handcrafted conditions or restrictions.

1 Introduction

Deep learning [Krizhevsky et al., 2012] dramatically has changed scientific fields such as computer vision, natural language processing, or the medical sciences. More recently, deep learning research has been expanded towards physical simulations such as fluid dynamics, deformable materials, or aerodynamics [Sanchez-Gonzalez et al., 2020, Pfaff et al., 2020]. The progress of deep learning in physical simulations was often driven by Graph Neural Networks (GNNs) [Scarselli et al., 2009, Defferrard et al., 2016, Kipf and Welling, 2017], which proved effective when modeling interactions between many entities via forward dynamics [Battaglia et al., 2018]. GNNs allowed the generalization

of fluid dynamics and 2D interactions over many time steps and different initial conditions [Sanchez-Gonzalez et al., 2020]. In Pfaff et al. [2020], GNNs learned mesh-based simulations to predict the dynamics of a wide range of physical systems, including aerodynamics and structural mechanics, as well as long-range interactions in N-body simulations [Martinkus et al., 2021].

However, typical engineering problems [Mayr et al., 2021] involve complex geometric boundaries, which cannot be modeled by cubic geometries as done in [Sanchez-Gonzalez et al., 2020], since such modeling quickly leads to insufficient precision. The conventional engineering approaches, which are based on a solid mathematical theory, model complex boundaries by triangularization leading to triangular meshes. In Fig. 1, examples of triangularized surfaces are shown for standard parts of many industrial machineries, namely a hopper (left) and a rotating drum (right). Machine learning methods have difficulties to handle such triangularized boundaries, since the constructed triangles are heterogeneous concerning their shapes, sizes, and orientations. In general, the accurate description of curved geometries requires a large number of triangles of different shapes and sizes (see e.g. Fig. 1 left). Consequently, many particle-boundary interactions must be considered, which is however often computationally not feasible for 3D problems.

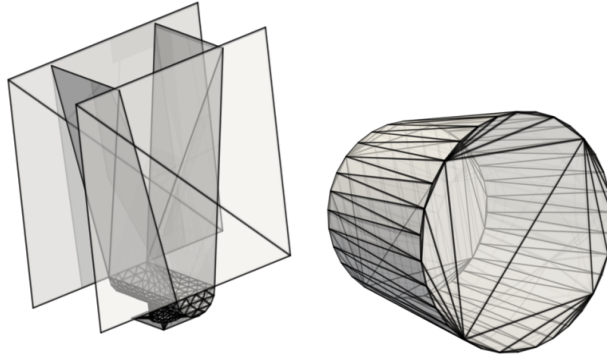


Figure 1: Triangularized boundary surfaces of hopper (left) and rotating drum (right). The accurate description of curved geometries requires a large number of triangles of different shapes and sizes.

We introduce Boundary Graph Neural Networks (BGNNs), which accurately model physical processes when triangularized boundary surfaces are present. BGNNs dynamically modify graph structures to model interactions of particles and triangulated boundaries. Boundary graph structures are constructed via modifying edges, augmenting node features, and inserting virtual nodes.

We test the effectiveness of BGNNs on complex 3D granular flow simulations of hoppers and rotating drums. Simulations of granular flow processes are required for the design of many industrial processes. Such simulations allow the optimization of devices and machinery in which particle flow is essential. Furthermore, these simulations are needed for a wide range of materials and material mixtures, which can have different cohesion properties and therefore for example appear as dry, wet, or oily.

The data for BGNN training is obtained by a precise but time-consuming simulation using the open-source Discrete Element Method (DEM) software LIGGGHTS¹ [Kloss et al., 2012]. The accuracy of our BGNN model is measured via aggregate quantities, namely averaged particle positions, flows, and mixing entropies. We ensure that our BGNN models have high simulation quality by requiring high accuracy of the models in terms of the aggregate quantities. BGNN predictions have the potential to be considerably faster than DEM methods while keeping the same precision. Code, training and test data will be made public upon publication.

The main contributions of this work are:

- We introduce Boundary Graph Neural Networks (BGNNs), which dynamically modify graph structures via boundary graph structures to allow an accurate modeling of particle interactions with and at triangularized boundaries.
- We implement BGNNs for learning complex 3D granular flow simulations of hoppers and rotating drums.

¹Licensed under the GNU GENERAL PUBLIC LICENSE.

- We assess the BGNN simulation quality via the difference of relevant physical quantities between prediction and simulated processes. We show that BGNNs are able to generalize granular flow dynamics over hundreds of thousands of timesteps while having the potential to be considerably faster than standard engineering methods.

2 Background and Related Work

Granular flow simulations. Granular flows are ubiquitous in nature and industrial processes. Pharmaceutical powders, plastic granulates, or rocks obtained by mining are just some examples of granular media that are used in industries and which are processed in a multitude of different flow states. While attempts have been made to formulate governing equations for granular flows, like the Navier-Stokes equations for fluid flow, they have so far eluded a general framework [Faccanoni and Mangeney, 2013]. The Discrete Element Method (DEM) [Cundall and Strack, 1979] avoids the necessity of an underlying governing equation and as such allows us the study of a wide variety of flow ranges and particle types. The key idea of DEM is to represent granular media by discrete objects, commonly referred to as particles (e.g. spheres or polyhedra). Particles interact by exchanging momentum at a particle-particle contact level using a contact model. The most basic contact model is a spring-dashpot model, in which the interaction force F_{ij} between two particles i and j is given as

$$F_{ij} = k \delta_{ij} - \gamma \dot{x}_{ij}, \quad (1)$$

where k is the spring stiffness, δ_{ij} is the overlap of the two particles, γ is the damping constant, and \dot{x}_{ij} is the relative velocity between two particles. We generate data for granular flow using simulations with the open-source DEM software LIGGGHTS [Kloss et al., 2012]. LIGGGHTS simulates particulate flows for a wide range of materials and complex mesh-based wall geometries and, therefore, enables the simulation of many industrial processes. Instead of complex mesh-based wall geometries, Sanchez-Gonzalez et al. [2020] use simpler static cuboids for 3D simulations. They use a material point method [Sulsky et al., 1995] based simulator [Hu et al., 2018] to model the boundaries and the interactions of particles. In contrast, our simulator utilizes the mesh to represent boundaries in a highly efficient way. Triangulated boundaries are not a unique feature of DEM. They are also employed in other meshless methods such as Smoothed Particle Hydrodynamics [Mayrhofer et al., 2015] which can be used for free surface flow simulations of the Navier-Stokes equations.

Time transition model. Similar to Sanchez-Gonzalez et al. [2020], a time-transition model is learned to predict particle accelerations. The time-transition from time t to time $t + 1$ is given by

$$\dot{x}^{t+1} = \dot{x}^t + \Delta t \ddot{x}^t, \quad (2)$$

$$x^{t+1} = x^t + \Delta t \dot{x}^{t+1}, \quad (3)$$

where x is the particle location, and \dot{x} the particle velocity. To calculate the time-transition x^{t+1} , the particle acceleration \ddot{x}^t is predicted.

Graph Neural Networks. We consider graphs $\mathcal{G} = (\mathcal{V}, \mathcal{E})$, with nodes $v_i \in \mathcal{V}$ and edges $e_{ij} \in \mathcal{E}$, where N -dimensional node features $\mathbf{p}_{v_i} \in \mathbb{R}^N$ are attached to each of the nodes. Whether the graph \mathcal{G} contains an edge between a pair of nodes (v_i, v_j) depends on the distance between the nodes

$$e_{ij} \in \mathcal{E} \iff d(v_i, v_j) \leq \text{cut-off}, \quad (4)$$

where the cut-off radius is usually a hyperparameter of the model. Edges might have M -dimensional edge features $\mathbf{a}_{ij} \in \mathbb{R}^M$ attached to each edge e_{ij} . Graph networks are designed to learn from graph-structured data [Scarselli et al., 2009, Kipf and Welling, 2017, Defferrard et al., 2016, Battaglia et al., 2018]. Message passing networks [Gilmer et al., 2017] are a specific type of graph neural networks and in most applications consist of three different types of layers: node and edge feature embedding layers, the core message passing layers, and read-out layers. The node feature embedding layers $\mathbf{h}_i = \psi(\mathbf{p}_{v_i})$ map the node features $\mathbf{p}_{v_i} \in \mathbb{R}^N$ to N' -dimensional node embeddings $\mathbf{h}_i \in \mathbb{R}^{N'}$. Similarly, edge features $\mathbf{a}_{ij} \in \mathbb{R}^M$ can be – but not always are – mapped via embedding layers $\mathbf{m}_{ij} = \phi(\mathbf{a}_{ij})$ to $\mathbf{m}_{ij} \in \mathbb{R}^{M'}$ edge embeddings. Message passing networks [Gilmer et al., 2017]

iteratively update node embeddings \mathbf{h}_i and edge embeddings \mathbf{m}_{ij} , also referred to as messages, at node v_i via the following steps:

$$\mathbf{m}'_{ij} = \Phi(\mathbf{h}_i, \mathbf{h}_j, \mathbf{m}_{ij}) , \quad (5)$$

$$\mathbf{m}'_i = \sum_{j \in \mathcal{N}(i)} \mathbf{m}'_{ij} , \quad (6)$$

$$\mathbf{h}'_i = \Psi(\mathbf{h}_i, \mathbf{m}'_i) , \quad (7)$$

where $\mathcal{N}(i)$ represents the set of neighbors of node v_i , and the learnable functions Φ and Ψ are commonly approximated by Multilayer Perceptrons (MLPs). Eq. (5)-(7) describe successively the computation and aggregating of messages, and the update of node embeddings. The final node embeddings are used for predictions via read-out layers, where depending on the task a pooling over all node embeddings can be applied.

3 Boundary Graph Neural Networks

Boundary Graph Neural Networks. We introduce Boundary Graph Neural Networks (BGNNs) for modeling the time transition dynamics in simulations within complex geometries. In BGNNs, each graph node v_i is associated to a particle with location \mathbf{x}_{v_i} , velocity $\dot{\mathbf{x}}_{v_i}$ and acceleration $\ddot{\mathbf{x}}_{v_i}$, which is similar to Sanchez-Gonzalez et al. [2020]. BGNNs modify and enhance the graph structure to include boundaries (see Fig. 2). BGNNs dynamically add \tilde{n} virtual nodes $\tilde{v}_j \in \tilde{\mathcal{V}}$ for boundary regions, iff the corresponding boundary region is within a cut-off radius to any other particle. We augment the set of edges \mathcal{E} by boundary edges \tilde{e}_{ij} giving an enhanced edge set $\tilde{\mathcal{E}}$ with $e_{ij} \in \mathcal{E}$ and $\tilde{e}_{ij} \in \tilde{\mathcal{E}}$. Analogously to Eq. (4), the existence of particle-particle edges e_{ij} and particle-boundary edges \tilde{e}_{ij} is determined via:

$$e_{ij} \in \mathcal{E} \iff d(v_i, v_j) \leq \text{cut-off}_e, \quad (8)$$

$$\tilde{e}_{ij} \in \tilde{\mathcal{E}} \iff \tilde{d}(v_i, \tilde{v}_j) \leq \text{cut-off}_{\tilde{e}}. \quad (9)$$

The cut-off radii cut-off_e and $\text{cut-off}_{\tilde{e}}$ do not have to be the same. In order to include more information about boundary surfaces into particle-boundary interactions, \tilde{N} -dimensional node features that encode information about the inclination of triangles in space are concatenated with the existing node features $\mathbf{p}_{v_i} \in \mathbb{R}^N$. Additionally, coordinate information is used both for existing nodes ($\mathbf{X} = \{\mathbf{x}_{v_0}, \dots, \mathbf{x}_{v_{n-1}}\}$) as well as for virtual nodes ($\tilde{\mathbf{X}} = \{\tilde{\mathbf{x}}_{\tilde{v}_0}, \dots, \tilde{\mathbf{x}}_{\tilde{v}_{\tilde{n}-1}}\}$). For virtual nodes, the additional coordinates $\tilde{\mathbf{x}}_{\tilde{v}_j}$ are chosen such that they minimize the distance to real particles. The resulting set of node features $\hat{\mathbf{P}}$ and node coordinates $\hat{\mathbf{X}}$ are:

$$\hat{\mathbf{P}} = \{\mathbf{p}_{v_0}, \dots, \mathbf{p}_{v_{n-1}}, \tilde{\mathbf{p}}_{\tilde{v}_0}, \dots, \tilde{\mathbf{p}}_{\tilde{v}_{\tilde{n}-1}}\} , \quad \hat{\mathbf{p}}_i \in \mathbb{R}^{N+\tilde{N}} , \quad (10)$$

$$\hat{\mathbf{X}} = \{\mathbf{x}_{v_0}, \dots, \mathbf{x}_{v_{n-1}}, \tilde{\mathbf{x}}_{\tilde{v}_0}, \dots, \tilde{\mathbf{x}}_{\tilde{v}_{\tilde{n}-1}}\} , \quad \hat{\mathbf{x}}_i \in \mathbb{R}^3 , \quad (11)$$

where $\hat{\mathbf{p}}_i$ and $\hat{\mathbf{x}}_i$ denote the elements of $\hat{\mathbf{P}}$ and $\hat{\mathbf{X}}$, respectively. Similarly to above, the node feature embedding layers $\hat{\mathbf{h}}_i = \hat{\psi}(\hat{\mathbf{p}}_i)$ map the $N + \tilde{N}$ -dimensional node features $\hat{\mathbf{p}}_i$ to N' -dimensional node embeddings. Edge features $\hat{\mathbf{a}}_{ij}$ for the edges e_{ij} and \tilde{e}_{ij} comprise edge features for particle-particle edges \mathbf{a}_{ij} and particle-boundary edges $\tilde{\mathbf{a}}_{ij}$. Edge features $\hat{\mathbf{a}}_{ij} \in \mathbb{R}^M$ are mapped via edge embedding layers $\hat{\mathbf{m}}_{ij} = \hat{\phi}(\hat{\mathbf{a}}_{ij})$ to M' -dimensional edge embeddings.

The message passing equations for the node embeddings $\hat{\mathbf{h}}_i$ and messages $\hat{\mathbf{m}}_{ij}$ read

$$\hat{\mathbf{m}}'_{ij} = \hat{\Phi}(\hat{\mathbf{h}}_i, \hat{\mathbf{h}}_j, \|\hat{\mathbf{x}}_i - \hat{\mathbf{x}}_j\|^2, \hat{\mathbf{x}}_i - \hat{\mathbf{x}}_j, \hat{\mathbf{m}}_{ij}) , \quad (12)$$

$$\hat{\mathbf{m}}'_i = \sum_{j \in \mathcal{N}'(i)} \hat{\mathbf{m}}'_{ij} , \quad (13)$$

$$\hat{\mathbf{h}}'_i = \hat{\Psi}(\hat{\mathbf{h}}_i, \hat{\mathbf{m}}'_i) , \quad (14)$$

where $\mathcal{N}'(i)$ represents the set of neighbors of the corresponding real or virtual node. In contrast to the message passing of Gilmer et al. [2017], the relative squared distances $\|\hat{\mathbf{x}}_i - \hat{\mathbf{x}}_j\|^2$ are included in

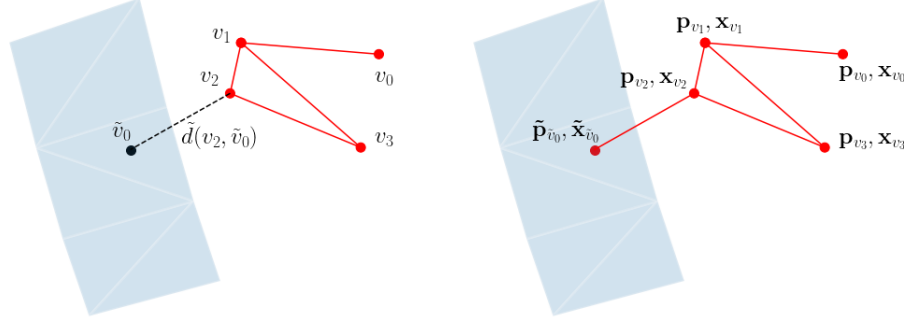


Figure 2: Left: Calculation of the distance $\tilde{d}(v_2, \tilde{v}_0)$ between a real particle at node v_2 and the triangle corresponding to virtual particle node \tilde{v}_0 . Right: Insertion of an additional edge between \tilde{v}_0 and v_2 and representation of the nodes in terms of the corresponding node features $\mathbf{p}_{v_i}, \mathbf{x}_{v_i}$ and $\tilde{\mathbf{p}}_{\tilde{v}_j}, \tilde{\mathbf{x}}_{\tilde{v}_j}$ for real and virtual node features, respectively.

the computation of messages in Eq. (12), similar as in Satorras et al. [2021]. Additionally, the relative differences $\hat{\mathbf{x}}_i - \hat{\mathbf{x}}_j$ are included. The final node embeddings are used for the predictions via the read-out layers. The main challenges of the implementation of BGNNs are the modification of the graph structure towards a **dynamic boundary graph structure** to include boundary information via the introduction of modified edges \tilde{e}_{ij} , modified node features $\hat{\mathbf{p}}_i$, and coordinates for virtual nodes $\tilde{\mathbf{x}}_{\tilde{v}_i}$. In the following section, we discuss how \tilde{e}_{ij} , $\hat{\mathbf{p}}_i$, and $\tilde{\mathbf{x}}_{\tilde{v}_i}$ are determined and calculated.

4 Dynamic Boundary Graph Structure

A boundary graph structure, which is a dynamic modification of the graph structure is needed for two reasons: (i) A static graph structure, which inserts many particles (number proportional to the surface area) for every boundary surface, would result in large computational costs in 3D scenes. (ii) For certain time frames, only some parts of the mesh might be relevant and computations can be saved. For example, as long as particles are in free fall in a container far away from the bottom, the mesh part describing the bottom is irrelevant for the next time step. A dynamic boundary graph structure is obtained in three stages:

- Calculating distances between real particles and triangular boundary surface areas in order to decide if a virtual particle node needs to be inserted into the graph, and subsequently obtain additional edges \tilde{e}_{ij} .
- Obtaining positional coordinates for virtual nodes $\tilde{\mathbf{x}}_{\tilde{v}_j}$ as representatives of the relevant fraction of the triangular surface area $\tilde{\mathbf{x}}_{\tilde{v}_j}$.
- Modifying node features $\hat{\mathbf{p}}_i$ by including normal directions to facilitate the learning of geometric relationships between particles and boundary surfaces.

Modified edges \tilde{e}_{ij} via calculation of distances to boundaries. To obtain modified edges \tilde{e}_{ij} , boundary particles are dynamically inserted, but only if a real particle is close to the corresponding boundary. The insertion of unnecessary edges into the graph is avoided. Such edges would connect nodes of real and virtual particles, though they are far apart. To decide whether a virtual particle has to be inserted requires the calculation of distances between pairs of real particles and mesh triangles. Specifically, the squared distance between the particle center and the closest point on the mesh triangles is calculated (adopted from [Eberly, 1999]). For this purpose, a location on a triangle \mathbf{t} is parametrized by two scalar values u and $v \in \mathbb{R}$:

$$\mathbf{t}(u, v) = \mathbf{b} + u \mathbf{e}_0 + v \mathbf{e}_1,$$

where $u \geq 0, v \geq 0$, and $u + v \leq 1$, \mathbf{b} represents one of the nodes of the triangle, and, \mathbf{e}_0 and \mathbf{e}_1 are vectors from \mathbf{b} towards the other two nodes (see Fig. 3). The minimal Euclidean squared distance q

of the point p to the triangle is given by the optimization problem:

$$\begin{aligned} \min_{u,v} \quad & q(u, v) = \|t(u, v) - p\|^2 \\ \text{s.t.} \quad & u \geq 0, \quad v \geq 0, \quad u + v \leq 1. \end{aligned} \quad (15)$$

The minimizing arguments u' and v' parametrize the closest point $t(u', v')$ of the triangle to the point p . As indicated in Fig. 3, seven cases have to be distinguished: one case (c0) in which $t(u', v')$ is located within the (closed) triangle, three cases (c1, c3, c5) in which $t(u', v')$ is located on one edge of the triangle (including the edge corner points as special cases), and three cases (c2, c4, c6) in which $t(u', v')$ is located on one of two edges (including the triangle corner points as special cases). Whether a virtual particle is inserted is determined by Eq. (9) and the particle-triangle distance q .

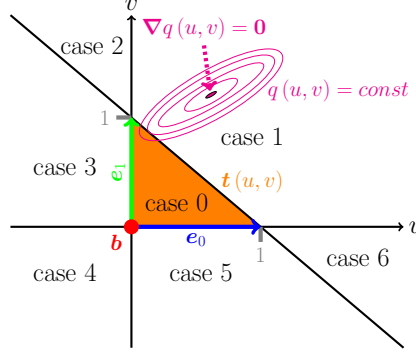


Figure 3: Visualization of point - triangle distance calculations in 3D. The triangle is represented by a parameterized function $t(u, v) = b + u e_0 + v e_1$ with $u \geq 0, v \geq 0, u + v \leq 1$ (indicated by the orange area). Level sets of $q(u, v)$ are indicated by ellipses and describe the squared Euclidean distance of a triangle point $t(u, v)$ to the point p , for which we compute the minimum distance.

Positional coordinates $\tilde{x}_{\tilde{v}_j}$ for virtual nodes. After having modified the edges \tilde{e}_{ij} via the calculation of distances between real particles and triangular boundary surface areas, we now have to decide where to place the virtual particles on these boundary surface areas. For virtual particles the coordinates $\tilde{x}_{\tilde{v}_j}$ correspond to $t(u', v')$, i.e., the closest points on the triangular boundary surface areas with respect to the interacting real particle.

Modifying node features \hat{p}_i by including boundary normal directions. Typical granular flow simulations comprise substantially more particle - particle interactions than particle - boundary interactions, which may impede the learning of particle - boundary interactions. In Kipf et al. [2018] the problem of qualitatively different interactions is addressed by introducing a dedicated message generating network for each interaction type. We avoid such extensions of our model by means of the following two approaches. First, we introduce additional node features, such that the neural network is able to distinguish the different types of nodes. Second, we adapted weight initialization of the node feature embedding $\hat{\psi}$, such that the embedding network could be trained with larger values for the additional features. Consequently, the network can learn different dynamics for particle - particle and particle - boundary interactions. The additional node features are: (i) type feature, i.e., a binary indicator of whether a node represents a particle that is real or virtual, and, in the latter case, (ii) the components of the normal vector of the triangular surface areas (null vectors for real particles).

There is however an ambiguity in the representation of planes via normal vectors due to the two possible orientations of the normal vectors, which correspond to the same geometry. In general, there are two possibilities of including normal vector information into the model: (i) encoding always that triangle plane normal vector which always points towards or away from the corresponding particle, (ii) including positively and negatively oriented versions of the normal vector, and order them. We decided for option (ii) since pathological cases where the particle is in the same plane as the triangle are avoided and training is further stabilized. In doing so, we have to deal with the fact that the network predictions should be invariant with respect to the orientation of the normal vectors. Therefore, we define a partial ordering which is able to sort the normal vectors with respect to their orientations. For a given normal vector $n = (n_1, n_2, n_3) \in \mathbb{R}^3$, we use the following partial order

function

$$f_o(\mathbf{n}) = \sum_{i=1}^3 3^{i-1} (\text{sgn}(n_i) + 1) \quad (16)$$

to retrieve the scalar values $f_o(\mathbf{n})$ and $f_o(-\mathbf{n})$ and sort the two vectors according to their corresponding mapped values. Different sign combinations of the normal vectors are shown in App. Fig. B.1. To test the performance of our approach, we conduct a toy experiment as well as a simulation experiment with different representations of normal vectors. We describe both experiments in App. B.1 and App. B.2.

5 Experiments

We test the effectiveness of BGNNs on complex 3D granular flow simulations. The development, design, and construction of many mechanical devices is based on granular flow simulations. These devices can have very different geometries and must be designed for a wide range of materials with highly varying properties. For example, cohesion properties can range from dry, wet, to oily. In the simulations, we consider very common device geometries and opposed cohesion properties to cover a wide range of situations with our available computational resources. The two common geometries are hoppers and rotating drums (see Fig. 1, Fig. 4, and Fig. 5). The two opposed cohesion properties are non-cohesive describing liquid-like, oily materials and cohesive describing dry sand-like materials. We compare the BGNN predictions to the simulations in two aspects: speed and accuracy.

Simulation Details. For all experiments, gravitation acts along the z -direction. The upper part of the hopper is delimited along the y -axis by two planes, which are parallel to the x - z plane (see Fig. 4). The x -axis is delimited by two planes, that are inclined at certain angles α , $180^\circ - \alpha$ to the x - y plane and at corresponding angles $\alpha - 90^\circ$, $90^\circ - \alpha$ to the y - z plane. The hopper has an initially closed hole at the bottom, which has an adjustable radius. The rotation axis of the drum is the y -axis (see Fig. 5). The initial filling of the hopper and drum is done by randomly inserting particles into a predefined region. More information can be found in App. C. We use around 1000 and around 3000 particles for hopper and rotating drum simulations, respectively. In order to have trajectories with non-cohesive and cohesive particles, we use the simplified JKR model [Roessler and Katterfeld, 2019] with a cohesion energy density of 0 J/m^3 and 10^5 J/m^3 for non-cohesive and cohesive particles. The training data consists of 30 simulation trajectories, where each trajectory consists of 100.000 (250.000) simulation timesteps for hopper (rotating drum). For BGNN training every 40 (100)-th timestep is used. The trajectories have different angles α and different hole radii for the hopper and different initial particle placement for the rotating drum. Moreover, the number of particles is varied by $\pm 25\%$.

Implementation Details. We use 5 message passing layers, with 128 and 512 nodes for intermediate node and edge representation. The cut-off radii strongly depend on the particle size. We use cut-off radii of 0.02 and 0.008 for rotating drum and hopper. Cut-off radii have been treated as hyperparameter of our model. Training takes about one day on a single NVIDIA A100 GPU. More details can be found in App. C.

Assessment Of Physical Quantities. Granular flow simulations should correctly describe systems on macroscopic scales in terms of **particle-averaged positions** $\bar{\mathbf{x}}(t)$ and **particle flows** $\bar{\mathbf{v}}(t)$ for n particles as a function of time: $\bar{\mathbf{x}}(t) = \frac{1}{n} \sum_i \mathbf{x}_i(t)$ and $\bar{\mathbf{v}}(t) = \frac{1}{n} \sum_i \mathbf{v}_i(t)$. Hoppers are devices that aim at adjusting the flow of particles along the direction of gravity, which coincides with the z -axis in our experiments. Rotating drums are commonly utilized as mixing devices for various applications in e.g. industry, research, and agriculture. They are essentially rotating cylinders that are partially filled with a granular material. The mixing property of these devices is a result of numerous particle interactions under time-varying boundary conditions. For rotating drum experiments, we quantify the extend of particle mixing via the **mixing entropy** [Lai and Fan, 1975]. If the z -coordinate of a particle's initial position $\mathbf{x}_i(0)$ is above (below) the median z -coordinate of all particles in the initial state, we assign it to class $c = +1$ (-1). Based on this assignment local entropies $s(\mathbf{g}_{klm}, t)$ at grid cells \mathbf{g}_{klm} are calculated, where the indices klm identify an individual grid cell. The local entropies $s(\mathbf{g}_{klm}, t)$ are computed from particle counts $n_c(\mathbf{g}_{klm}, t)$, of the respective classes $c = \pm 1$. The total number of particles in a grid cell is obtained by $n(\mathbf{g}_{klm}, t) = n_{+1}(\mathbf{g}_{klm}, t) + n_{-1}(\mathbf{g}_{klm}, t)$. Calculating

the particle-number weighted average of the local mixing entropies yields the mixing entropy $S(t)$ of the entire system:

$$S(t) = \frac{-1}{\sum_{klm} n(\mathbf{g}_{klm}, t)} \sum_{klm} \sum_{c=\pm 1} n(\mathbf{g}_{klm}, t) (f_c(\mathbf{g}_{klm}, t) \log f_c(\mathbf{g}_{klm}, t)), \quad (17)$$

where $f_c(\mathbf{g}_{klm}, t)$ denotes the relative fraction of class c particles in cell \mathbf{g}_{klm} at time t .

Results. In Fig. 4 and Fig. 5 results for hopper and rotating drum simulations are presented. The left parts visualize granular flow snapshots at different time steps, both for cohesive and non-cohesive materials. The right parts of the figures include average position and particle flow plots for hopper, as well as particle flow and mixing entropy plots for rotating drum simulations. The simulation uncertainties arise due to the different distributions of the initial filling and due to a $\pm 25\%$ difference in the number of particles across simulations. Short video clips of the trajectories are added as supplement. Cohesive and non-cohesive particles behave quite differently.

BGNNs have learned to model granular flow simulations over thousands of time steps. Most notably, hardly any particle leaves the geometric boundaries. This is achieved without using handcrafted conditions or restrictions on the positions of the particles. BGNNs have learned to model particle-boundary interactions and in doing so correctly represent the physics within the system. The predicted quantities are within uncertainties of the simulations, therefore we consider the BGNN predictions as sufficiently precise to substitute the simulations.

Table 1 gives a run-time comparison of the LIGGGHTS simulation versus a forward pass of BGNNs, which only predict every 100 time steps. The highly optimized CPU algorithm (LIGGGHTS) and a non-optimized GPU compatible algorithm (BGNNs) are compared via their wall-clock times since the hardware settings are quite different. Nevertheless, Tab. 1 shows that the wall-clock time of BGNNs is shorter than the wall-clock time of the simulation. The usage of more particles, would further increase the lead of BGNNs over the simulation in terms of wall-clock time. For the time comparison, we use a typical simulation trajectory from our datasets with 3,408 particles, which needs approximately 2 GB GPU memory for one forward path. There is potentially even more space for improvement of the BGNN predictions over simulations due to the so called **Young’s modulus**. For simulations, it is often assumed that energy is purely transmitted through Rayleigh waves, thus the time step of DEM simulations is targeted to be a fraction of the propagation time through a single, solid particle. As such the propagation time depends on material parameters, most notably the Young’s modulus. However, for several materials the Young’s moduli that reflect the true material properties, would lead to extremely small propagation times, which in turn means much more simulation steps. Consequently, much smaller Young’s moduli are considered as approximation, which is valid for gravity driven flows [Coetzee, 2017]. However, for many cases, e.g. the penetration of particle bed by an object, this approximation breaks down [Lommen et al., 2014]. BGNNs have the potential to be trained on very small time steps reflecting the true Young’s moduli and consequently generalize over much more than “just” 40 or 100 time steps.

method	device	specification	time steps	wall-clock time [s]
LIGGGHTS	CPU	AMD EPYC 7H12	1	356
BGNNs	GPU	NVIDIA A100	100	158

Table 1: Runtime comparison for one granular flow process consisting of 250.000 simulation timesteps, which are 2500 BGNN predictions.

6 Limitations and conclusion

Limitations. We have shown that BGNNs are able to accurately reproduce 3D granular flows without using handcrafted conditions or restrictions. However, successful simulations often require precise hyperparameter tuning. The supplement material contains examples of unsuccessful runs for all reported settings where a slight change of hyperparameters yields unstable predictions. Currently, BGNNs are limited when modeling granular flows with many particles and long range interactions. For example, we have so far only used 30 trajectories consisting of several thousand simulation timesteps each. Finally, we have so far not touched materials with high Young’s moduli, and thus

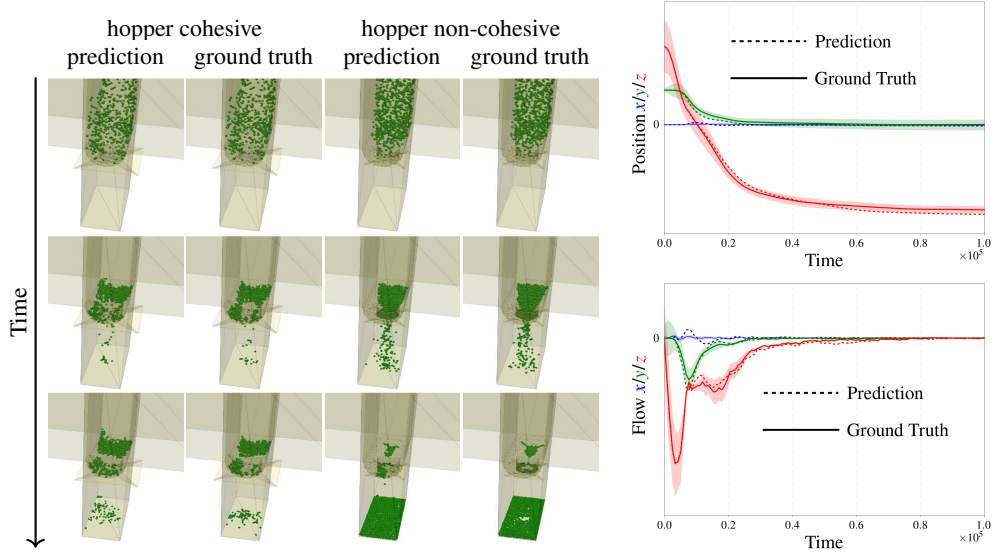


Figure 4: Left: Distributions for hopper dynamics for cohesive and non-cohesive particles. Simulation data and BGNN predictions are compared. Particles are indicated by green spheres, triangular wall areas are yellow, the edges of these triangles are indicated by grey lines. In contrast to liquid-like non-cohesive particles, cohesive particles lead to congestion of the hopper. Right: Position (upper right) and flow profile (lower right) for non-cohesive particles. Corresponding plots for cohesive particles can be found in App. C. Simulation data (solid lines) and BGNN predictions (dashed lines) are compared. Simulation uncertainties are due to a change of the particle numbers ($\pm 25\%$) and to different initial conditions.

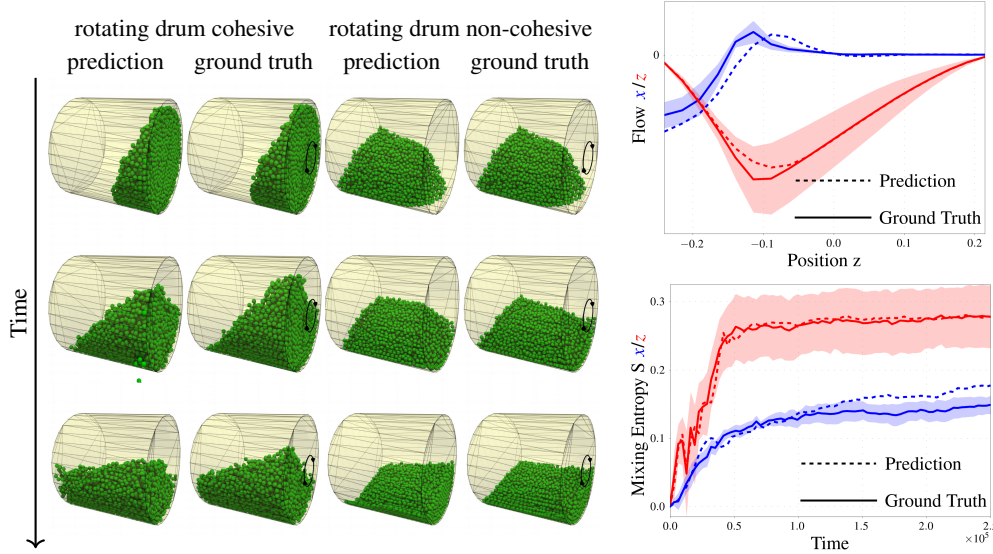


Figure 5: Left: Particle distributions for rotating drum dynamics for cohesive and non-cohesive particles. Simulation data and BGNN predictions are compared. Particles are indicated by green spheres, triangular wall areas are yellow, the edges of these triangles are indicated by grey lines. The circular arrow indicates the rotation direction of the drum. In contrast to liquid-like non-cohesive particles, cohesive particles stick together much stronger. Right: position (upper right) and entropy plot (lower right) for non-cohesive particles. The entropy is shown for particle class assignment according to the x (blue) and z (red) position. Corresponding plots for cohesive particles can be found in App. C. Simulation data (solid lines) and BGNN predictions (dashed lines) are compared. Simulation uncertainties are due to a change of the particle numbers ($\pm 25\%$) and to different initial conditions.

we have not yet tested the generalization properties of BGNNs for such scenarios as described in Sec. 5. For a broader impact, we would like to stress that BGNNs are inherently suited for modeling a wide range of particle dynamics, and as such are prone to be used without reflection. Relying on simulations always requires rigorous monitoring, especially when simulations are learned, which can be considered as a second order modeling scheme. Nevertheless, the societal impact of BGNN simulations is hardly predictable, as it strongly depends on the purpose of the simulated experiments.

Conclusion. We have introduced Boundary Graph Neural Networks (BGNNs) in order to achieve an accurate neural network modeling of simulated physical processes with complex geometries. BGNNs dynamically modify graph structures via modifying edges, augmenting node features, and dynamically inserting virtual nodes. We have tested BGNNs on complex 3D granular flow processes of hoppers and rotating drums, where BGNNs are able to accurately reproduce 3D granular flows within simulation uncertainties over hundreds of thousands of timesteps, and most notably particles stay within the geometric objects without using handcrafted conditions or restrictions.

Acknowledgments

This research was supported by FFG grant 871302 (DL for granular flow).

The ELLIS Unit Linz, the LIT AI Lab, the Institute for Machine Learning, are supported by the Federal State Upper Austria. IARAI is supported by Here Technologies. We thank the projects AI-MOTION (LIT-2018-6-YOU-212), DeepToxGen (LIT-2017-3-YOU-003), AI-SNN (LIT-2018-6-YOU-214), DeepFlood (LIT-2019-8-YOU-213), Medical Cognitive Computing Center (MC3), PRIMAL (FFG-873979), S3AI (FFG-872172), ELISE (H2020-ICT-2019-3 ID: 951847), AIDD (MSCA-ITN-2020 ID: 956832). We thank Janssen Pharmaceutica (MaDeSMart, HBC.2018.2287), Audi.JKU Deep Learning Center, TGW LOGISTICS GROUP GMBH, Silicon Austria Labs (SAL), FILL Gesellschaft mbH, Anyline GmbH, Google, ZF Friedrichshafen AG, Robert Bosch GmbH, UCB Biopharma SRL, Merck Healthcare KGaA, Software Competence Center Hagenberg GmbH, TÜV Austria, and the NVIDIA Corporation.

We thank Angela Bitto-Nemling and Markus Holzleitner for helpful discussions and comments on this work.

References

- J.L. Ba, J.R. Kiros, and G.E. Hinton. Layer normalization. *arXiv preprint arXiv:1607.06450*, 2016.
- P.W. Battaglia, J.B. Hamrick, V. Bapst, A. Sanchez-Gonzalez, V.F. Zambaldi, M. Malinowski, A. Tacchetti, D. Raposo, A. Santoro, R. Faulkner, Ç. Gülçehre, H.F. Song, A.J. Ballard, J. Gilmer, G.E. Dahl, A. Vaswani, K.R. Allen, C. Nash, V. Langston, C. Dyer, N. Heess, D. Wierstra, P. Kohli, M. Botvinick, O. Vinyals, Y. Li, and R. Pascanu. Relational inductive biases, deep learning, and graph networks. *arXiv preprint arXiv:1806.01261*, 2018.
- N. Bonneel, M. van de Panne, S. Paris, and W. Heidrich. Displacement interpolation using lagrangian mass transport. 30(6):1–12, December 2011. ISSN 0730-0301. doi: 10.1145/2070781.2024192.
- CJ Coetzee. Calibration of the discrete element method. *Powder Technology*, 310:104–142, 2017.
- P.A. Cundall and O.D.L. Strack. A discrete numerical model for granular assemblies. *Geotechnique*, 29(1):47–65, 1979.
- M. Defferrard, X. Bresson, and P. Vandergheynst. Convolutional neural networks on graphs with fast localized spectral filtering. In D. Lee, M. Sugiyama, U. Luxburg, I. Guyon, and R. Garnett, editors, *Advances in Neural Information Processing Systems*, volume 29. Curran Associates, Inc., 2016.
- D. Eberly. Distance between point and triangle in 3d. Retrieved from <http://www.magic-software.com/Documentation/pt3tri3.pdf>, 1999.
- G. Faccanoni and A. Mangeney. Exact solution for granular flows. *International Journal for Numerical and Analytical Methods in Geomechanics*, 37(10):1408–1433, 2013.
- R. Flamary and N. Courty. Pot python optimal transport library, 2017. URL <https://pythonot.github.io/>.
- J. Gilmer, S.S. Schoenholz, P.F. Riley, O. Vinyals, and G.E. Dahl. Neural message passing for quantum chemistry. In *International Conference on Machine Learning*, pages 1263–1272. PMLR, 2017.
- K. He, X. Zhang, S. Ren, and J. Sun. Delving deep into rectifiers: Surpassing human-level performance on imagenet classification. In *Proceedings of the 2015 IEEE International Conference on Computer Vision (ICCV)*, page 1026–1034, 2015.
- K. He, X. Zhang, S. Ren, and J. Sun. Deep residual learning for image recognition. In *Proceedings of the IEEE Conference on Computer Vision and Pattern Recognition (CVPR)*, June 2016.
- Y. Hu, Y. Fang, Z. Ge, Z. Qu, Y. Zhu, A. Pradhana, and C. Jiang. A moving least squares material point method with displacement discontinuity and two-way rigid body coupling. *ACM Transactions on Graphics*, 37(4), July 2018. ISSN 0730-0301.
- W. Kahan. Pracniques: further remarks on reducing truncation errors. *Communications of the ACM*, 8(1):40, 1965.
- D.P. Kingma and J.L. Ba. Adam: A method for stochastic gradient descent. pages 1–15, 2015.
- Thomas Kipf, Ethan Fetaya, Kuan-Chieh Wang, Max Welling, and Richard Zemel. Neural relational inference for interacting systems. In *International Conference on Machine Learning*, pages 2688–2697. PMLR, 2018.
- Thomas N. Kipf and Max Welling. Semi-supervised classification with graph convolutional networks. In *International Conference on Learning Representations (ICLR)*, 2017.
- A. Klein. A generalized kahan-babuška-summation-algorithm. *Computing*, 76(3-4):279–293, 2006.
- C. Kloss, C. Goniva, A. Hager, S. Amberger, and S. Pirker. Models, algorithms and validation for opensource dem and cfd-dem. *Progress in Computational Fluid Dynamics, An International Journal*, 12(2/3):140, 2012. ISSN 1468-4349.
- C. Kloss, A. Aigner, A. Mayrhofer, and C. Goniva. fastdem: A method for faster dem simulations of granular media. In *Particles 2017*, 2017.

- A. Krizhevsky, I. Sutskever, and G.E. Hinton. Imagenet classification with deep convolutional neural networks. *Advances in Neural Information Processing Systems*, 25:1097–1105, 2012.
- F.S. Lai and L.T. Fan. Application of a discrete mixing model to the study of mixing of multicomponent solid particles. *Industrial & Engineering Chemistry Process Design and Development*, 14(4):403–411, 1975. doi: 10.1021/i260056a009.
- S. Lommen, D. Schott, and G. Lodewijks. Dem speedup: Stiffness effects on behavior of bulk material. *Particuology*, 12:107–112, 2014.
- K. Martinkus, A. Lucchi, and N. Perraudin. Scalable graph networks for particle simulations. *arXiv preprint arXiv:2010.06948*, 2021.
- A. Mayr, S. Lehner, A. Mayrhofer, C. Kloss, S. Hochreiter, and J. Brandstetter. Learning 3d granular flow simulations. *arXiv preprint arXiv:2105.01636*, 2021.
- A. Mayrhofer, M. Ferrand, C. Kassiotis, D. Violeau, and F.-X. Morel. Unified semi-analytical wall boundary conditions in sph: analytical extension to 3-d. *Numerical Algorithms*, 68(1):15–34, 2015.
- J. Mellmann, K.L. Iroba, T. Metzger, E. Tsotsas, C. Mészáros, and I. Farkas. Moisture content and residence time distributions in mixed-flow grain dryers. *Biosystems Engineering*, 109(4):297–307, 2011.
- V. Nair and G.E. Hinton. Rectified linear units improve restricted boltzmann machines. In *International Conference on Machine Learning*, page 807–814, 2010.
- T. Pfaff, M. Fortunato, A. Alvaro Sanchez-Gonzalez, and P.W. Battaglia. Learning mesh-based simulation with graph networks, 2020.
- S. Plimpton. Fast parallel algorithms for short-range molecular dynamics. *Journal of computational physics*, 117(1):1–19, 1995.
- T. Roessler and A. Katterfeld. Dem parameter calibration of cohesive bulk materials using a simple angle of repose test. *Particuology*, 45:105–115, 2019.
- A. Sanchez-Gonzalez, J. Godwin, T. Pfaff, R. Ying, J. Leskovec, and P. Battaglia. Learning to simulate complex physics with graph networks. In *Proceedings of the 37th International Conference on Machine Learning*, volume 119, pages 8459–8468, 2020.
- V. G. Satorras, E. Hoogeboom, and M. Welling. E (n) equivariant graph neural networks. *arXiv preprint arXiv:2102.09844*, 2021.
- F. Scarselli, M. Gori, A.C. Tsoi, M. Hagenbuchner, and G. Monfardini. The graph neural network model. *IEEE Transactions on Neural Networks*, 20(1):61–80, 2009.
- D. Sulsky, S.J. Zhou, and H.L. Schreyer. Application of a particle-in-cell method to solid mechanics. *Computer Physics Communications*, 87(1-2):236–252, 1995.

A Discrete Element Method (DEM) simulator LIGGGHTS

The open source DEM software LIGGGHTS [Kloss et al., 2012] is based on the Molecular Dynamics code LAMMPS [Plimpton, 1995] developed by Sandia National Labs. Due to the similarity of the underlying algorithms for neighbor list construction, output and parallelism this provided a stable basis for the contact models required for DEM. LIGGGHTS added support for triangular mesh walls, particle insertion and new particle shapes (multispheres and superquadrics). Several of those changes resulted in upstream contributions in LAMMPS.

Over the years LIGGGHTS has become a widely used software in both academia and industry that supports both cutting edge research and industrial applications. Support for several physical phenomena as, e.g. liquid transfer on particles, was instrumental in its success. However, it also highlighted requirements for additional research. In industrial applications there often is the need to study physical phenomena which occur on different time scales, e.g. particle collisions ($O(10^{-5}s)$) vs. moisture content in particles ($O(1s)$, [Mellmann et al., 2011]), which can lead to weeks of simulation time. While advances have been made to overcome such issues (e.g. [Kloss et al., 2017]), they remain limited in their application, due to the fact that they rely on prior simulation of the exact setup and cannot be used for interpolation of quantities directly related to the flow behavior.

In 2019 LIGGGHTS was again forked and forms the basis of the commercial DEM software Aspherix® which expands the capabilities of LIGGGHTS with polyhedral particles, a significantly simplified input language and graphical user interface.

B Normal Vector Representations

As described in the main paper, for a given normal vector $\mathbf{n} = (n_1, n_2, n_3) \in \mathbb{R}^3$, we use the following partial order function

$$f_o(\mathbf{n}) = \sum_{i=1}^3 3^{i-1} (\text{sgn}(n_i) + 1) \quad (\text{B.1})$$

to retrieve the scalar values $f_o(\mathbf{n})$ and $f_o(-\mathbf{n})$ and sort the two vectors according to their corresponding mapped values. Different sign combinations of the normal vectors are shown in Fig. B.1. To test the performance of our approach, we conduct a toy experiment as well as a simulation experiment with different representations of normal vectors. We describe both experiments in App. B.1 and App. B.2.

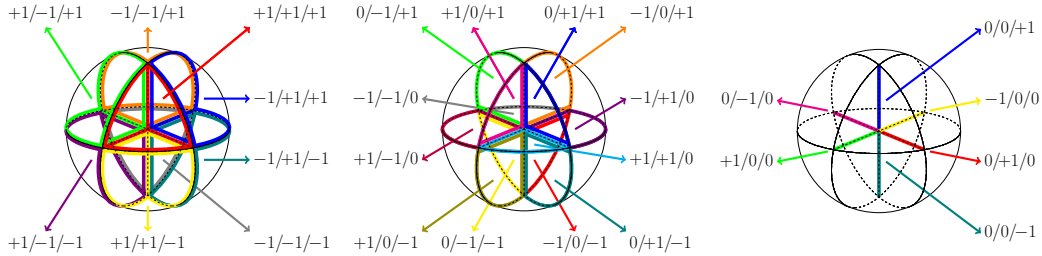


Figure B.1: Partial ordering of normal vectors. The numbers indicate the signs of normal vector components, which are used in the partial order function. The figures from left to right visualize different (ordered) sign combinations. Sets of sign combinations without zero values form volumes (left), sets with one zero value form planar areas (middle), and sets with two zero values form line sections (right). The 0/0/0 combination forms a point at the origin.

B.1 Reflection Toy Example

We conduct a toy experiment to showcase that a partial ordering of normal vectors is helpful for learning 3D simulations. In detail, we consider reflection (*Ref*) at a plane \mathbf{n} as given by

$$\text{Ref}_{\mathbf{n}}(\mathbf{v}) = \mathbf{v} - 2 \frac{\mathbf{v} \cdot \mathbf{n}}{\mathbf{n} \cdot \mathbf{n}} \mathbf{n}, \quad (\text{B.2})$$

and try to learn the reflection formula by a simple ReLU network, which takes the 3 components of \mathbf{n} and \mathbf{v} as input features and predicts the 3 components of $Ref_{\mathbf{n}}(\mathbf{v})$. The training data consists of reflections at four fixed walls: the top, the bottom, the left, and, the right side of a simple cube.

We use normal vectors of these walls, that point towards the inner of the cube. When evaluating the performance of the trained models, we observe decent predictions, if the orientation of the normal vectors describing the inclination of the walls was equal to the training data (see R1-R4 in Fig. B.2). However, for inverted normal vectors in the test set, only networks which take a partial ordering of the normal vectors into account predict the reflection correctly (see R3, R4 in Fig. B.3).

B.2 Simulation Experiment

We compare three different versions of how to include normal vector information for the hopper particle flow experiments:

- not including normal vector information, and filling six node features up with zero entries instead (V1)
- including single normal vector orientation, which is given by the triangle corner point order of the mesh (V2)
- including both normal vector orientations (six features) (V3).

From an information perspective, it should be noted that (i) distance information (scalar distance and relative distance vectors) to the walls is present in the edge features of the graph and (ii) in most cases the used normal vectors are oriented towards the outside of relevant border walls.

The different particle distribution trajectories obtained by the three versions are compared by computing the Earth Movers distances [Bonneel et al., 2011, Flamary and Courty, 2017, EMD] of predicted and simulated trajectories. We use Euclidean distances for the cost matrix, which we compute at time steps $2^0, 2^1, \dots, 2^{16}$ for 5 training trajectories and 5 test trajectories. Table B.1 shows the means (μ) and standard deviations (σ) of EMD values at different time steps and from 5 different training and test trajectories. A paired Wilcoxon test on the concatenated trajectories, shows that V3 significantly outperforms V1 (p-value 2.42e-04) and V2 (p-value 1.50e-03) on the test data.

Interestingly, there is less significance on the training data, which might indicate that the usage of orientation-independent features to represent walls, helps to improve generalization performance, while it might not be that helpful for optimization purposes alone.

Table B.1: Usage of different normal vector information in hopper particle flow experiment. The table summarizes means (μ) and standard deviations (σ) of the EMD for the different versions and shows the results of a paired Wilcoxon test.

Version		Train			Test		
		μ	σ	p-value Row < V3	μ	σ	p-value Row < V3
V1	No normal vector	5.06e-05	1.17e-04	2.36e-02	6.80e-05	1.59e-04	2.42e-04
V2	Single normal vector	1.15e-04	3.84e-04	3.40e-03	1.21e-04	4.33e-04	1.50e-03
V3	Both orientations	5.99e-05	1.77e-04		6.36e-05	2.06e-04	

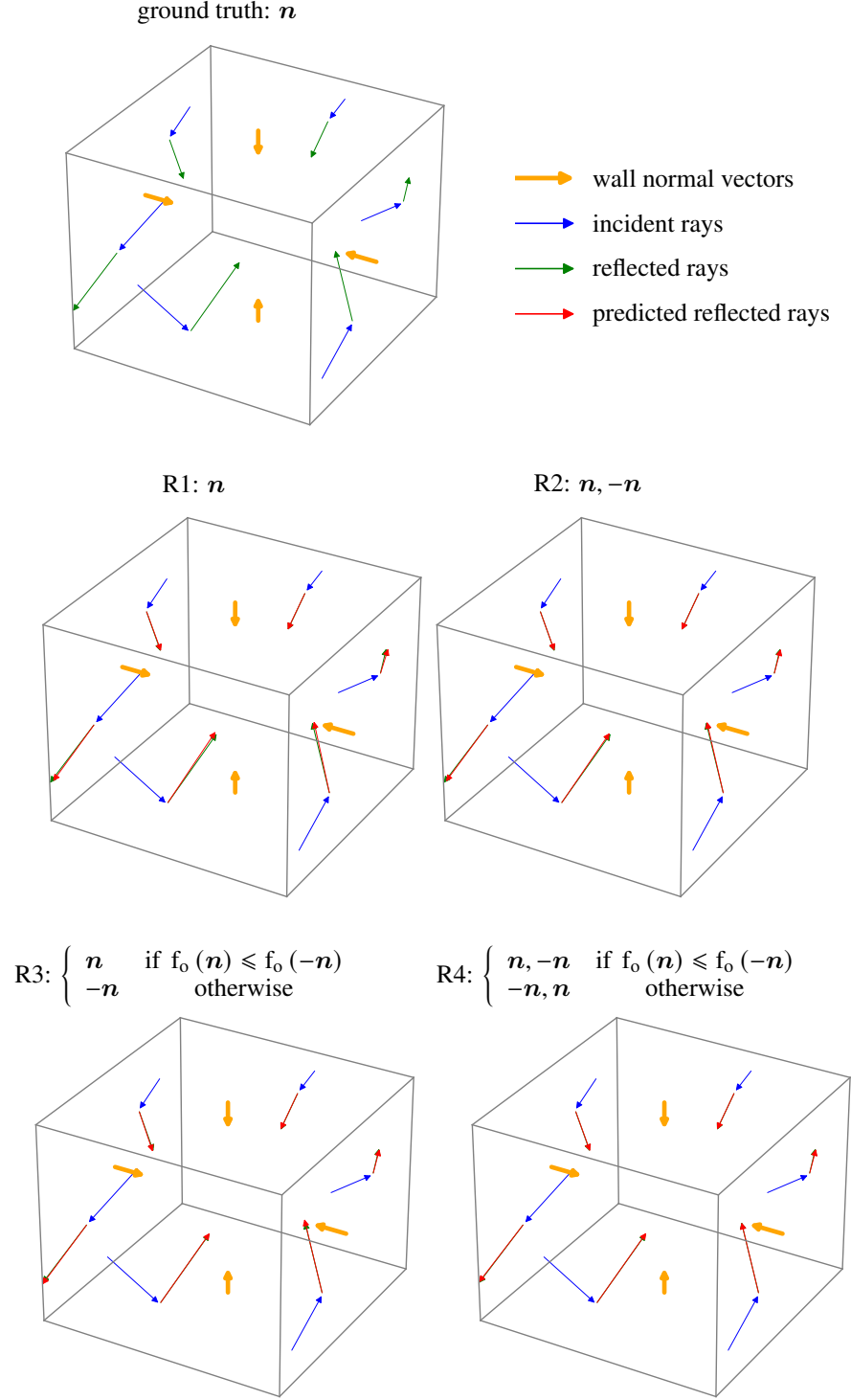


Figure B.2: Reflection of rays at four different walls (left, right, bottom, top). Wall normal vectors are visualized by bold orange arrows. The incident rays are visualized by blue arrows, reflected rays by green arrows, and neural network predictions by red arrows. Neural network predictions are based on wall representations **that are oriented the same way as in the training phase**. The caption above each plot indicates the wall input features used for training each of the networks.

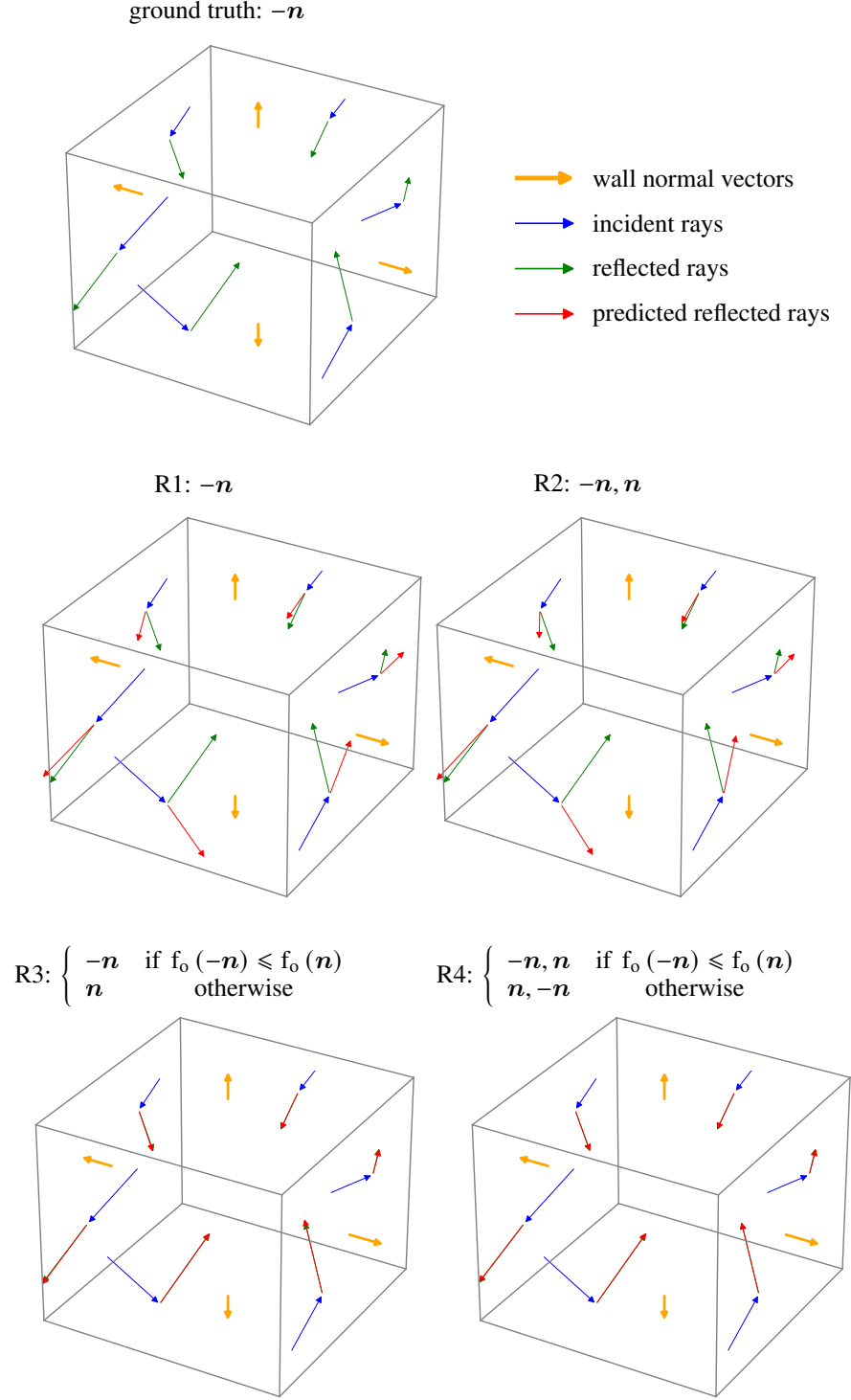


Figure B.3: Reflection of rays at four different walls (left, right, bottom, top). Wall normal vectors are visualized by bold orange arrows. The incident rays are visualized by blue arrows, reflected rays by green arrows, and neural network predictions by red arrows. Neural network predictions are based on wall representations **that are inversely oriented compared to the training phase**. The caption above each plot indicates the wall input features used for training each of the networks.

C Experiments

C.1 Simulation details

Hopper The initialization consists of two phases. In a first step, particles are randomly inserted into a small cuboid which is positioned at a certain height above the closed hole of the hopper. This cuboid is continuously filled with particles during the initialization phase and afterwards particles freely move downwards (along the direction of gravity). In this way, the hopper is filled up to a certain height with 20,000 particles. In a second phase, we cut out particles from the filled mass of particles. We do this (i) by applying randomly selected functions and by (ii) randomly filtering out particles from the whole particle mass. The randomly selected functions are e.g. hyperplanes, where we only keep particles if they are at the same side of the hyperplane. The inserted particles have a radius of 0.002 m.

Drum For initialization we assume that the direction of gravity is different than the usual gravitation direction. We insert particles at two random fixed regions within the drum. After the particles are inserted, they can move according to the gravitation direction during the initialization phase. In this way, we obtain different initial particle distributions within the drum. The inserted particles have a radius of 0.01 m.

C.2 Implementation details

Graph Neural Network We use residual connections [He et al., 2016] for both node and edge updates. For both updates, we use simple two-layer MLP networks, ReLUs [Nair and Hinton, 2010] after the first layer, and layer normalization [Ba et al., 2016] without an additional activation after the second layer. For layer normalization we consider the ϵ -parameter as a hyperparameter and set it to 1.0. The networks for input embedding and read-out are similar to the message passing layers without layer normalization. The network weights are initialized similar to He et al. [2015]; for the input embeddings we assume an increased number of input neurons for `fan_in`, where we consider the additional neurons as virtual copies of e.g. the wall indication feature in order to be able to upweight the influence of these features. We use the mean-squared error as an objective and train with Adam optimization [Kingma and Ba, 2015]. In order to facilitate learning, we provide as hyperparameter options not only $\|\hat{\mathbf{x}}_i - \hat{\mathbf{x}}_j\|^2$, $\hat{\mathbf{x}}_i - \hat{\mathbf{x}}_j$ as features to the network, but also $\frac{1}{\|\hat{\mathbf{x}}_i - \hat{\mathbf{x}}_j\|}$, $\frac{\hat{\mathbf{x}}_i - \hat{\mathbf{x}}_j}{\|\hat{\mathbf{x}}_i - \hat{\mathbf{x}}_j\|^2}$ and $\frac{1}{\|\hat{\mathbf{x}}_i - \hat{\mathbf{x}}_j\|^2}$, $\frac{\hat{\mathbf{x}}_i - \hat{\mathbf{x}}_j}{\|\hat{\mathbf{x}}_i - \hat{\mathbf{x}}_j\|^3}$ reflecting the inverse distance law and the inverse-square law, which are present in many physical laws. We normalize input and target vectors and use a variant of Kahan summation [Kahan, 1965, Klein, 2006] in order to compute numerically stable statistics across particles of our dataset.

Hyperparameter Selection We keep 5 trajectories for each setting aside for validation. Criteria for hyperparameter selection are (i) that particles stay within the geometric object, and (ii) that the ground truth trajectory is reproduced.

C.3 Experimental Results For Cohesive Material

In the following, experimental results for a cohesive material are shown. The results in the main paper are obtained for non-cohesive granular material, i.e. material with a cohesion energy density of 0 J/m^3 , which results in liquid-like behaviour. Increasing the cohesion energy density to 10^5 J/m^3 corresponds to cohesive granular material, i.e. the particles have a strong tendency to clump together. Figure C.1 shows the corresponding comparison of physical quantities for the cohesive granular material. Like in the non-cohesive case, the predictions for cohesive granular material are widely in agreement with the ground truth simulation.

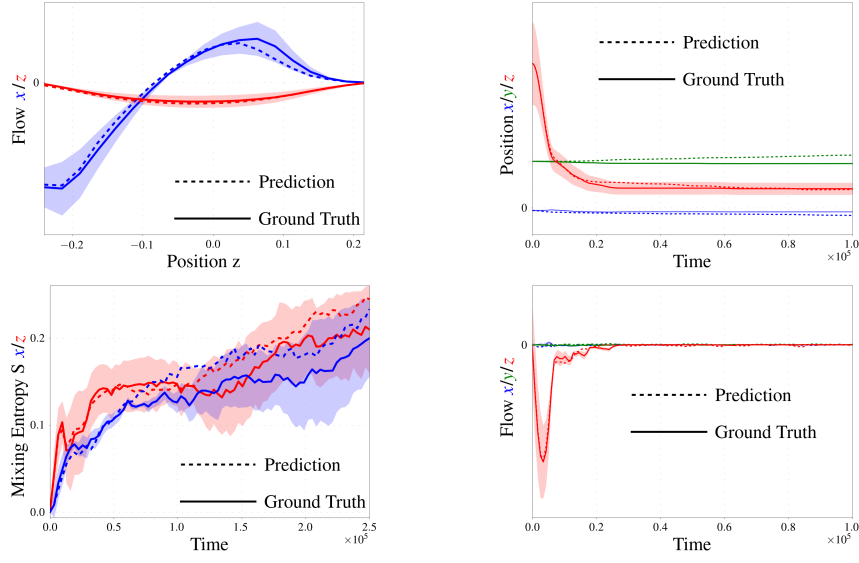


Figure C.1: Experimental results for cohesive granular material. Left, top: Time integrated particles flow in rotating drum in the x and z direction as a function of the position along the z axis. Left, bottom: Mixing entropies in the rotating drum as a function of time for particle class assignments according to the x (blue) and z (red) position. Right, top and bottom: Average particle position and particle flows for the hopper as a function of time.